




Cite this: *RSC Adv.*, 2025, 15, 40368

# Development of magnesium-doped zinc oxide nanopowders for conductometric acetone gas sensors

M. El Beji,<sup>a</sup> N. Hafiene,<sup>a</sup> M. Jdir,<sup>a</sup> S. Jaballah,<sup>a</sup> M. N. Bessadok,<sup>a</sup> <sup>a</sup> F. Ben Ali,<sup>a</sup> G. Neri<sup>b</sup> and L. El Mir \*<sup>a</sup>

This research investigates magnesium-doped zinc oxide nanoparticles (NPs) synthesised by a modified sol-gel technique to create a high-performance gas sensing device with an enhanced sensing layer. The synthesised nanoparticles' structural, morphological characteristics, composition, and optical properties were analysed using X-ray diffraction (XRD), transmission electron microscopy (TEM), scanning electron microscopy (SEM), energy-dispersive spectrometry (EDX), UV-Vis absorption, and photoluminescence spectroscopy (PL). XRD analysis depicts that the samples possessed a hexagonal crystal structure with high crystallinity. TEM and SEM analyses indicated that the nanoparticle size was approximately 45 nm, and this size increased with the increasing magnesium content. The gas sensor evaluations were performed in the temperature range from 200 to 400 °C. The ZnO sample that was doped with 1% Mg (M1ZO) demonstrated the greatest response (~19.9) to 40 ppm acetone (C<sub>3</sub>H<sub>6</sub>O) at 300 °C. This sensor exhibited quicker response and recovery times, ranging from 2 to 332 s, respectively, alongside enhanced selectivity for C<sub>3</sub>H<sub>6</sub>O when compared to ammonia (NH<sub>3</sub>), carbon dioxide (CO<sub>2</sub>), hydrogen sulphide (H<sub>2</sub>S), and sulphur dioxide (SO<sub>2</sub>). These findings suggest that Mg-doped ZnO holds promise as a material for controlling pollution and for applications in environmental gas sensing.

Received 15th July 2025  
Accepted 13th October 2025

DOI: 10.1039/d5ra05067g

rsc.li/rsc-advances

## 1. Introduction

Acetone is commonly used as a solvent in industrial, pharmaceutical, and household settings, presenting significant risks to both environmental and human well-being.<sup>1</sup> As a volatile organic compound (VOC), acetone can readily evaporate and contribute to atmospheric pollution, participating in the formation of ground-level ozone and secondary organic aerosols, which in turn affect air quality and contribute to climate change.<sup>2</sup> Breathing in acetone vapours, particularly in inadequately ventilated spaces, can result in immediate health issues, including irritation of the respiratory tract, headaches, dizziness, and nausea. Long-term exposure could cause more severe problems, such as liver and kidney dysfunction. Due to these risks, ongoing and accurate tracking of acetone levels in both ambient air and exhaled breath is crucial. This has sparked considerable interest in developing highly sensitive, selective, and fast-responding acetone sensors, particularly for environmental monitoring applications. Among various sensing materials,<sup>3–7</sup> metal oxide semiconductors, particularly zinc oxide (ZnO),<sup>8</sup> have demonstrated exceptional promise in

enhancing gas-sensing effectiveness. ZnO has been widely used as a sensing material for detecting various gases due to its distinctive characteristics, which include a large bandgap (3.37 eV), excellent electron mobility, thermal stability, and significant surface reactivity.<sup>9,10</sup> These traits enable ZnO to be especially efficient in identifying volatile organic compounds at minimal concentrations. Nonetheless, pure ZnO sensors typically require high operating temperatures,<sup>11</sup> generally exceeding 400 °C, to achieve sufficient sensitivity and response times, thereby limiting their practical applications and increasing energy consumption. To address these limitations, scientists have investigated different doping methods, incorporating external metal ions into the ZnO lattice to alter its electronic configuration, surface characteristics, and catalytic performance. Doping ZnO with elements like magnesium (Mg),<sup>12</sup> gallium (Ga),<sup>13</sup> or aluminium (Al)<sup>14</sup> has been demonstrated to greatly improve its gas sensing abilities by lowering the operating temperature, boosting sensitivity, and enhancing selectivity for specific target gases such as acetone. Mg-doped ZnO has shown encouraging results due to its ability to tune the charge carrier density and improve the adsorption-desorption dynamics,<sup>15</sup> which are key parameters for good gas detection at moderate temperatures. The main charge carriers in ZnO, an n-type semiconductor, are electrons. Defects like oxygen vacancies are introduced by doping with magnesium, and these serve as active sites for gas adsorption. These flaws improve sensitivity

<sup>a</sup>Gabes University, Faculty of Sciences of Gabes, Laboratory of Physics of Materials and Nanomaterials Applied at Environment (LaPhyMNE), 6072 Gabes, Tunisia. E-mail: Lassaad.ElMir@fsg.rnu.tn

<sup>b</sup>Department, of Engineering, University of Messina, C. da Di Dio, 98166 Messina, Italy



and selectivity by altering charge carrier behavior and increasing the number of reactive sites.

In this work, we developed acetone ( $\text{C}_3\text{H}_6\text{O}$ ) gas sensors using Mg-doped ZnO materials, which exhibit exceptional efficiency at 300 °C. Even at very low quantities of  $\text{C}_3\text{H}_6\text{O}$  gas around 5 ppm, these sensors exhibit high sensitivity, quick response and recovery times. In this regard, the effect of magnesium doping was systematically investigated to enhance ZnO's gas sensing properties by altering its surface shape and energy band structure. Mg doping was used as a tool to enhance the structural and electrical properties of ZnO, creating active centres enabling optimal sensor performances at around 300 °C.

## 2. Experiments

### 2.1. Synthesis of the samples

The procedure for synthesising ZnO:Mg nanoparticles was as follows: 16 g of zinc acetate dihydrate [ $\text{Zn}(\text{CH}_3\text{COO})_2 \cdot 2\text{H}_2\text{O}$ ; 99%] was dissolved in 112 mL of methanol using a magnetic stirrer for 10 minutes. Next, a suitable amount of magnesium nitrate dihydrate [ $\text{Mg}(\text{NO}_3)_2 \cdot 2\text{H}_2\text{O}$ , 98%] relating to  $[\text{Mg}]/([\text{Zn}] + [\text{Mg}])$  ratios of 0.01 (M1ZO), 0.03 (M3ZO), and 0.05 (M5ZO) were added to the above solution while maintaining magnetic stirring as shown in Fig. 1 for an additional 15 minutes until achieving a clear and uniform solution. After the precursors had fully dissolved, 188 mL of ethanol was added. This solution was then transferred into an autoclave and dried under the supercritical conditions of ethyl alcohol ( $T_c = 243$  °C,  $P_c = 63.6$  bars) following the method described by El Mir *et al.*<sup>16,17</sup> Additionally, the acquired samples were subjected to heat treatment at 450 °C in air for 2 hours in a furnace to produce well-crystallised Mg-doped ZnO nanopowders. In the following, we indicate the samples by MXZO with X denoting the atomic percentage of Mg relative to Zn.

### 2.2. Characterisation

To examine the crystal structure, morphology, and crystallite size of the synthesised samples, a variety of characterisation techniques were utilised. X-ray diffraction (XRD) was employed to identify the phase composition and crystallographic structure, whereas transmission electron microscopy (TEM) offered in-depth information about the morphology and particle size. Furthermore, UV-Vis absorption and photoluminescence (PL) spectroscopy were employed to assess the optical properties and defect states of the materials. X-ray diffraction measurements were performed using a Bruker AXS D8 Advance diffractometer. The average size of the crystallites ( $D$ , in Å) was calculated using the Williamson–Hall method, which relies on the broadening of the diffraction peaks.<sup>18</sup> Additionally, the strain of the lattice is a significant factor contributing to the broadening of the sample's diffraction peaks. Williamson and Hall developed a method to study the width of the diffraction peaks.<sup>19</sup> This method relates the expansion caused by size ( $\beta_e$ ) to the increase caused by stress ( $\beta_L$ ), as shown in eqn (1) and (2):

$$\beta_{\text{tot}} = \beta_e + \beta_L \quad (1)$$

$$\beta_{\text{tot}} \cos \theta = \frac{K\lambda}{D} + C\varepsilon \sin \theta \quad (2)$$

where  $\varepsilon$  represents the lattice strain,  $\lambda$  (1.5418 Å) is the wavelength of  $\text{CuK}\alpha$  radiation, and  $D$  is the crystallite size,  $K$  is the shape factor (0.9). The morphology of the samples was analysed using a field emission scanning electron microscope (FESEM, type) and transmission electron microscope (TEM; Tecnai G2-200 kV). Elemental composition was analysed using energy-dispersive X-ray (EDX) spectroscopy. Porosity characteristics (*i.e.*, pore diameter and volume) and specific Brunauer–Emmett–Teller (BET) surface area were estimated using an ASAP 2020 Micromeritics analyser, based on adsorption–desorption

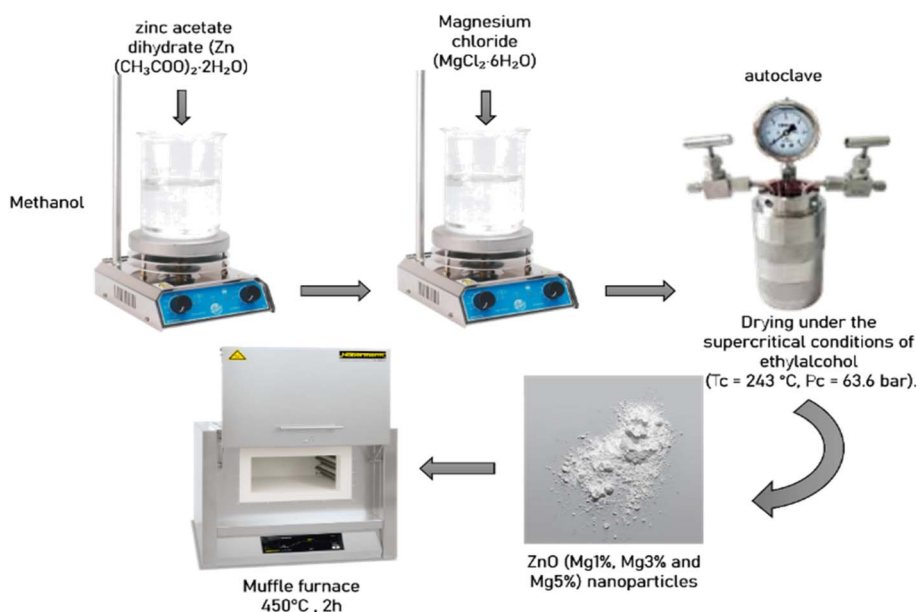


Fig. 1 Schematic illustration of the MXZO nanopowders prepared by the modified sol–gel technique.





Fig. 2 A detailed schematic showing how the gas sensing system is configured.

isotherms of  $N_2$  at 77 K. The sample was outgassed at 250 °C for 6 h in a vacuum at the beginning of each analysis. The surface area was calculated from the BET equation. The volume of micropores and surface area of mesopores were calculated from the t-plot method of Lippens and de Boer.<sup>20</sup> The optical characterisation was investigated with a UV-Vis-NIR spectrophotometer (Shimadzu UV-3101PC). Photoluminescence (PL) measurements were performed employing a Horiba NanoLog modular spectrofluorometer, using a Xenon (Xe) lamp as the excitation light source. The samples were excited by a wavelength of 340 nm, and the emission spectra were captured within the range of 340 to 900 nm. X-ray photoelectron spectrometry (XPS) using a Thermo Fisher Scientific K-Alpha spectrometer fitted with a monochromatic aluminium  $K\alpha$  radiation source ( $h\nu = 1486.6$  eV), and to examine the chemical composition, a 400 mm X-ray spot was applied.

### 2.3. Acetone sensing measurements

Sensor devices were created by mixing Mg-doped ZnO samples with water to produce a paste, which was subsequently screen-printed onto alumina substrates (3 mm × 6 mm) that had been pre-patterned with interdigitated platinum (Pt) electrodes and a heater. Before the sensing tests, the sensors underwent conditioning in air for 2 hours at 450 °C. Electrical measurements were taken over a temperature range from 200 to 400 °C. Sensing tests were executed using a laboratory setup that could regulate the temperature while conducting resistance measurements (Fig. 2), with different concentrations of  $C_3H_6O$  gas introduced into the carrier stream. The tests were carried out in dry synthetic air with a total flow rate of 100 sccm, and the sensor resistance data were gathered employing a four-point measurement method with an Agilent 34 970 A multimeter. The gas reaction was determined as  $S = R_a/R_g$ , in which  $R_a$  indicates the sensor's electrical resistance in dry air, while  $R_g$  denotes the resistance at different concentrations of  $C_3H_6O$  gas.

## 3. Results and discussion

### 3.1. Structural and morphological properties

The microstructural examination of nanopowders produced after thermal treatment at 450 °C for 2 hours has been carried out by XRD. The obtained results indicated that Mg-doped ZnO nanopowders exhibit high crystallinity, clearly demonstrated by the prominent peaks observed between 30 and 70° as shown in Fig. 3, attributed to the (100), (002), (101), (111), (200), (102) facets of the hexagonal wurtzite ZnO structure ( $P6_3mc$ ) according to the standard JCPDS data card n° 36-1451.<sup>21</sup>

The refined XRD patterns of synthesised ZnO and MXZO nanoparticles are shown in Fig. 4. The experimental XRD patterns are shown in red, and the fitted graphs are shown in black. Bragg's positions are shown by vertical green lines, and the difference between experimental and fitted lines is shown by

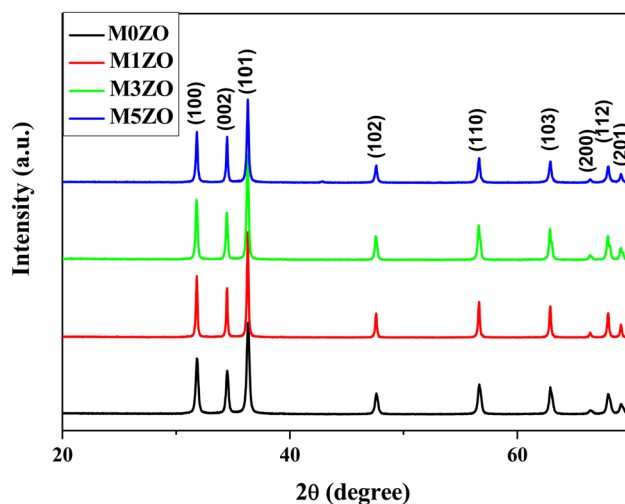


Fig. 3 X-ray diffraction analysis of ZnO, M1ZO, M3ZO, and M5ZO samples heat-treated at 450 °C for 2 hours.



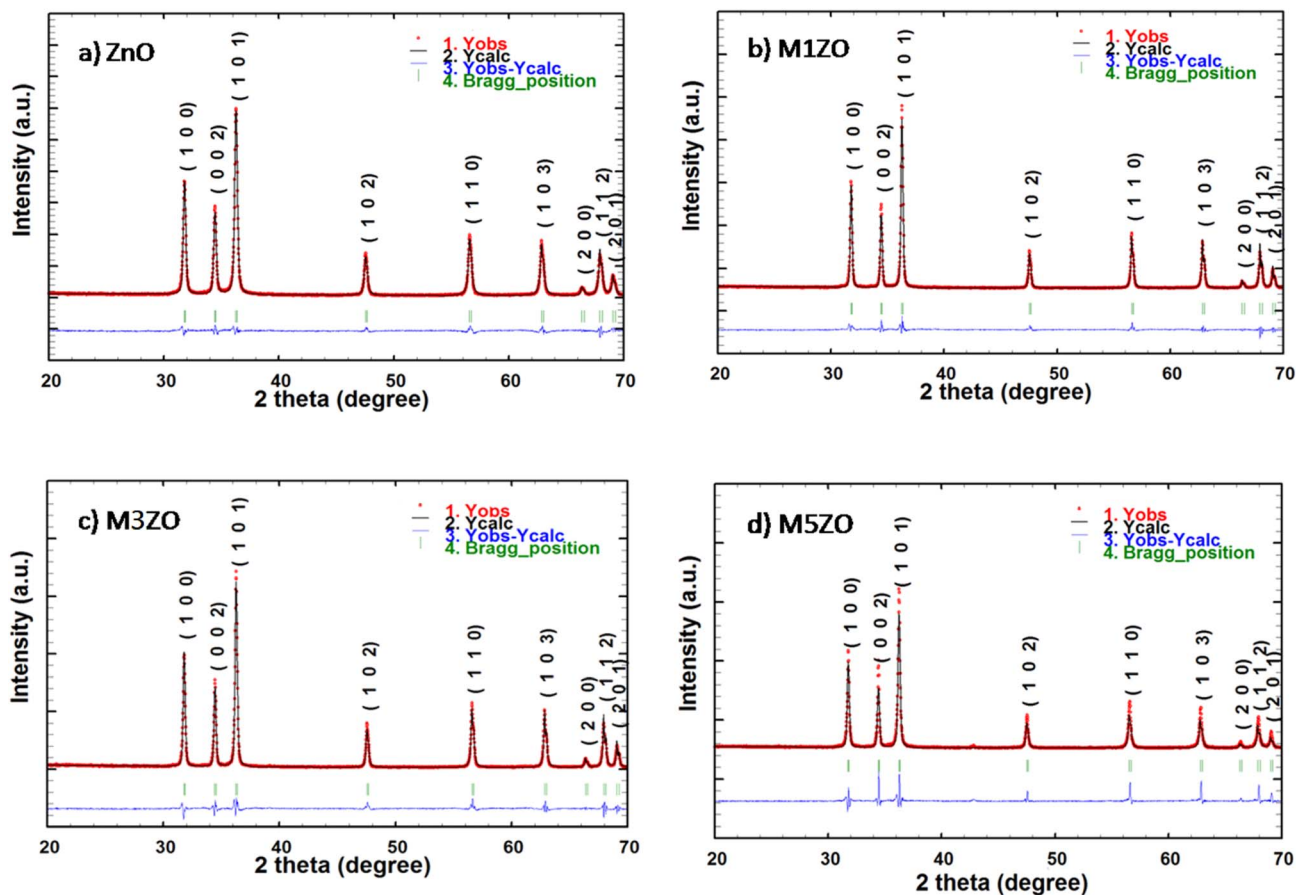


Fig. 4 Refined XRD patterns of ZnO and MXZO nanoparticles.

a blue line. It can be observed that the fitted graph is in good agreement with the experimental one.

Table 1 summarises the different refined lattice constants and unit cell volumes. The refined lattice constants of the ZnO sample are in good agreement with the literature ( $a = 0.3249$  nm,  $c = 0.5206$  nm).<sup>22</sup> The increase of lattice parameters for MXZO samples and hence the expansion of the corresponding unit cell volume is confirmed.

The Williamson–Hall (W–H) plots for each synthesised material are shown in Fig. 5. It is noteworthy that the Williamson–Hall relationship was used to determine the strain ( $\epsilon$ )

and the average crystal size ( $D$ ). For the undoped ZnO sample, the approximate average crystal size was 38 nm for samples M1ZO, M3ZO, and M5ZO; the values were 43, 47, and 56 nm, respectively. The nucleation process and the increase in surface energy of the MXZO NPs may be responsible for this increase.<sup>22,23</sup> Table 1 shows the crystallographic information of ZnO and MZO nanoparticles and the size of the crystallites.

Table 1 Crystallographic data analysis of pure and Mg-doped ZnO nanoparticles

Sample	Lattice parameters (Å)	Lattice volume (Å <sup>3</sup> )	$D$ W–H (nm)	Strain ( $\epsilon$ ) ( $10^{-4}$ )
ZnO	$a = 3.24614$ $c = 5.20184$	47.48	38	9.24
M1ZO	$a = 3.24984$ $c = 5.20609$	47.618	43	10.30
M3ZO	$a = 3.24969$ $c = 5.20594$	47.612	47	9.92
M5ZO	$a = 3.25228$ $c = 5.20970$	47.722	56	9.01

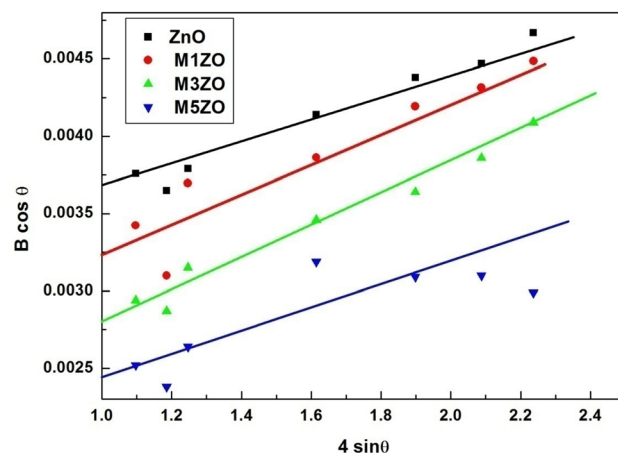


Fig. 5 Williamson Hall plots of ZnO and MXZO nanoparticles.



Incorporating Mg into ZnO nanoparticles appears to increase their crystal size. In addition, as shown in the table, the estimated strain value of MXZO is in the same order of magnitude as that of ZnO. The slight variation in ionic radii between  $\text{Zn}^{2+}$  ( $\sim 0.74 \text{ \AA}$ ) and  $\text{Mg}^{2+}$  ( $\sim 0.72 \text{ \AA}$ ) might be responsible for this result.<sup>24,25</sup>

Fig. 6 depicts SEM images of MXZO nanopowders. The samples show dispersed spherical aggregates with gradual increase in density as function of Mg loading.

Fig. 7 shows TEM images of Mg-doped ZnO samples that have been heat-treated for two hours at  $450^\circ\text{C}$ . As demonstrated, the magnesium-doped ZnO material has a prismatic

shape with an average size in the range of 40–60 nm. The TEM images' descriptions of the nanoparticle sizes for M1ZO, M3ZO and M5ZO agree with the XRD results.

The isotherm shape provides information on pore size, which is typically categorised as micropore, mesopore, or macropore. Fig. 8 depicts the evolution of  $\text{N}_2$  adsorption-desorption isotherms for MXZO nanopowders. These isotherms were obviously type II, with a hysteresis of H4 type, according to the IUPAC classification of sorption isotherms<sup>20</sup> (formerly designated as Brunauer's classification). At elevated relative pressure  $P/P_0$ , the hysteresis of H4 type was due to the filling up

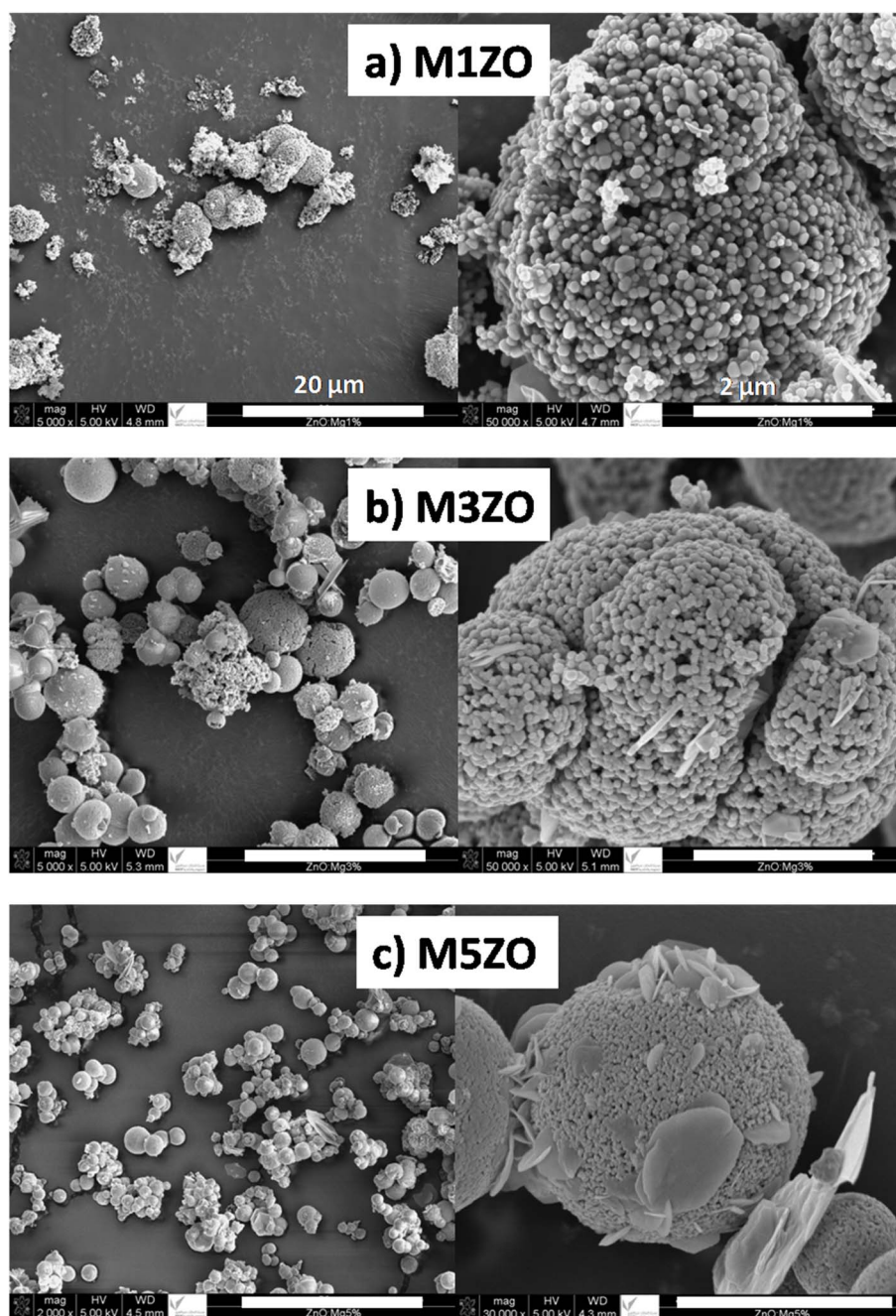


Fig. 6 SEM images of (a) M1ZO, (b) M3ZO and (c) M5ZO showing micrometric spherical aggregates formed of nanoparticles.



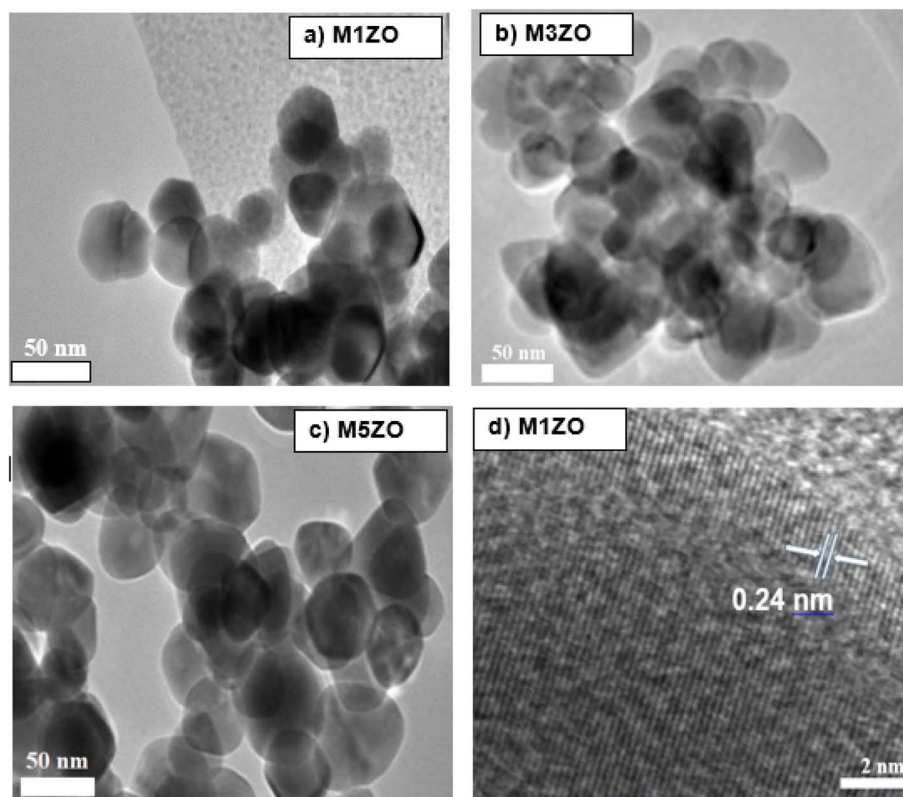


Fig. 7 TEM images showing the morphology of the nanosized Mg-doped ZnO samples: (a) M1ZO, (b) M3ZO, (c) M5ZO, and (d) magnified image for the M1ZO sample. The doped ZnO nanoparticles have a prismatic shape with an average size in the range of 40–60 nm.

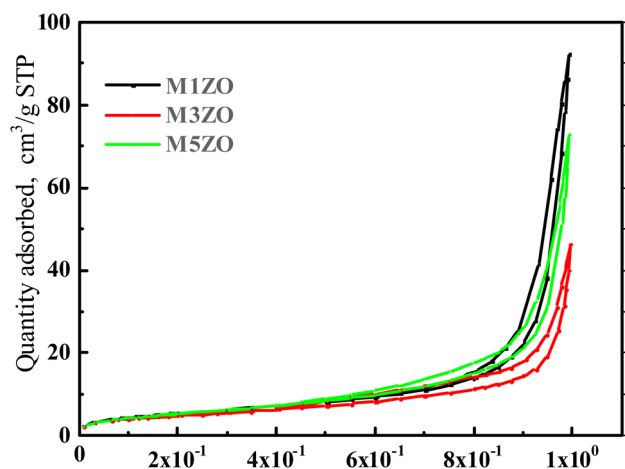


Fig. 8 Adsorption-desorption isotherms of  $N_2$  at 77 K of pure and Mg-doped zinc oxide nanopowders.

of mesopores by capillary condensation, indicating a shape of pores that was flatter instead of cylindrical.

Particle size, pore characteristics, and BET surface area are listed in Table 2. BET surface area was found to be about  $20 \text{ m}^2 \text{ g}^{-1}$  for the Mg-doped Samples, and the highest value was obtained for the M1ZO sample.

Results showed decreased mean diameter of pores in the range (from 24.2 nm to 12.2 nm) and total volume ( $14.5 \times 10^{-2}$

$\text{cm}^3 \text{ g}^{-1}$  to  $6.3 \times 10^{-2} \text{ cm}^3 \text{ g}^{-1}$ ) for samples with doping ratio ranging from 1% to 5%. Al Dahoudi *et al.*<sup>26</sup> have reported a very similar trend of BET surface area for crystalline IZO nanopowder synthesized by hydrothermal treatment. They observed that the incorporation of indium ions into ZnO particles obviously affected both the growth of ZnO lattice and nanostructure. They further demonstrated an evolution of nanoparticle shape, *i.e.*, rod-like pure ZnO progressively transformed to spherical, thereby leading to decreased nanoparticle size with increased indium-doping concentration.

The band gap energy is calculated based on the Tauc relation.<sup>27,28</sup> Fig. 9 shows the plot of  $(\alpha h\nu)^2$  vs.  $(h\nu)$ , which gives the  $E_g$  values of all samples when the linear region is extrapolated to the x-axis. The estimated bandgap values are 3.22, 3.23 and 3.17 eV, respectively, for M1ZO, M3ZO, and M5ZO samples. The bandgap energy slightly increases for 1% and 3% Mg dopant and then decreases. Several studies<sup>29–32</sup> reported an increase in the bandgap energy of ZnO with the addition of the Mg dopant.

Table 2 Main characteristics of MXZO nanopowders

Nanoparticles	Pore diameter (nm)	Pore volume ( $\text{cm}^3 \text{ g}^{-1}$ ) $\times 10^2$	Surface BET ( $\text{m}^2 \text{ g}^{-1}$ )
M1ZO	24.2	14.5	20.07
M3ZO	18.3	11.5	19.51
M5ZO	12.2	6.3	17.92



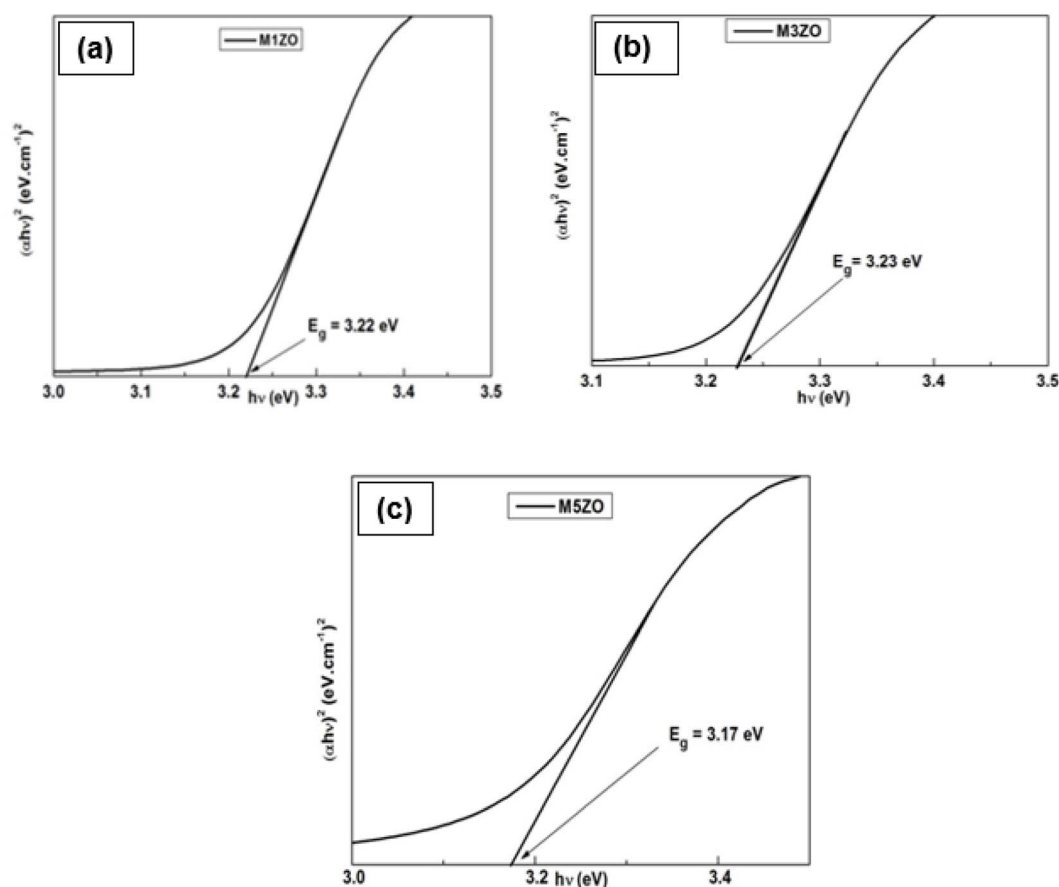


Fig. 9 Determination of the bandgap energy of Mg-doped ZnO nanoparticles.

This broadening of bandgap is most likely attributed to the Moss–Burstein effect. Lu *et al.*<sup>33</sup> reported that, if the Fermi surface was supposed spherical, the gap energy would be given as follows:

$$E_g = E_g^0 + \Delta E_g^{\text{BM}} \quad (3)$$

where,  $E_g$  and  $E_g^0$  are the band gap energies of doped and undoped ZnO, respectively and  $\Delta E_g^{\text{BM}}$  is the energy band gap widening. The band gap widening is related to the electron concentration and given according to the following Burstein–Moss equation:<sup>34</sup>

$$\Delta E_g = \frac{h^2}{2m_{\text{vc}}^*} (3\pi^2 n)^{\frac{2}{3}} \quad (4)$$

where  $h$  is Planck's constant,  $n$  is the carrier concentration, and  $m_{\text{vc}}^*$  is the reduced effective mass carrier. Indeed, an increase in carrier concentrations induces a shift of the Fermi level towards the conduction band and thus widens the energy band gap. The decrease in band gap for the M5ZO sample might be due to the presence of a secondary phase, which was further confirmed in XRD results. Similar behaviour was found by Kulandaisamy *et al.* and was attributed to the high number of defects.<sup>35</sup>

Fig. 10(a) shows the photoluminescence patterns of ZnO nanoparticles with different Mg loadings at room temperature.

The photoluminescence spectrum consists of two bands: a narrow ultraviolet (UV) emission band at 380 nm and a broad visible emission band at 554 nm. The UV emission corresponding to an energy of 3.26 eV, very close to the ZnO bandgap, is due to band-to-band recombination, *i.e.* a transition of an electron from the conduction to the valence band. While the second emission in the visible range corresponding to an energy of about 2.24 eV has generated much discussion and is generally attributed to oxygen vacancies  $\text{V}_{\text{O}}$ .<sup>36,37</sup> The evolution of PL intensity with Mg content confirms that Mg has been successfully incorporated into the ZnO lattice. The intensity of the green emission band decreases with Mg content from 1 to 5 at%. This emission observed in ZMO samples is mainly due to oxygen vacancies, which are intrinsic defects in the lattice. This behaviour agrees well with the results of elemental analysis, where the increase in the Mg concentration corresponds to a decrease in the oxygen vacancy content. Oxygen vacancies enhance the adsorption and reaction of target gas molecules such as acetone on the ZnO surface. Therefore, the intensity of the green emission is related to the defect concentration, which in turn directly affects the gas sensing of ZnO-based materials. In addition, Gaussian fitting deconvolution to the broad visible band (Fig. 10(b)–(d)), reveals, in addition to the main peak corresponding to the oxygen vacancy, two more contributions at 477 nm (blue-green region) and 660 nm (red region) for all



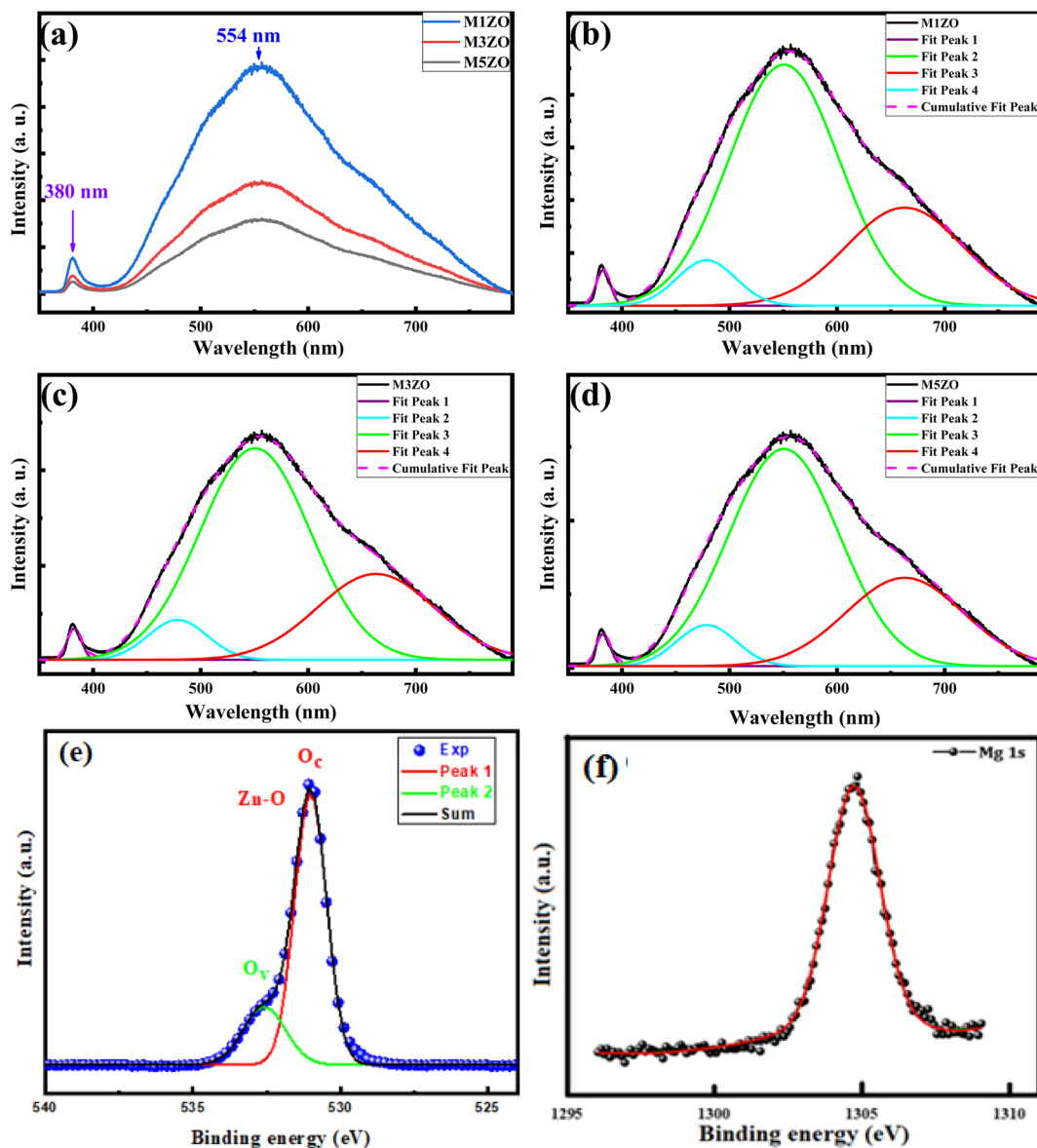


Fig. 10 (a) Room temperature PL spectra of different Mg-doped ZnO samples. The deconvolution of 1, 3 and 5 at% Mg loading percentages are presented respectively in (b), (c) and (d). XPS spectra of M1ZO nanopowder, (e) Zn–O and O<sub>v</sub>; (f) Mg 1s.

samples. Such emissions are known for ZnO samples and are mainly due to zinc vacancy ( $V_{Zn}$ ) and oxygen interstitial ( $O_i$ ) intrinsic defects.<sup>38</sup> In fact, the presence of such defects can play a predominant role in enhancing the gas sensing properties, such as lowering the response/recovery time and improving the selectivity toward some gases.

The spectrum in Fig. 10(e) showed the high-resolution O 1s XPS of the M1ZO sample, which could be fitted by two peaks: one (marked by  $O_c$ ) located at 530.77 eV, considered to be caused by the lattice  $O^{2-}$  anion in the Zn–O bond, and another (marked by  $O_v$ ) at 532.30 eV, related to the oxygen vacancy defects.<sup>38</sup> The relative concentration of oxygen vacancies ( $O_v/(O_v + O_c)$ ) can be estimated semi-quantitatively by its area ratio in the O 1s XPS curves, which could be expressed as 13% of  $O_v$  and 87% of  $O_c$ . The results confirm that the used

protocol enhances oxygen vacancy formation, which is beneficial for the creation of active centres and strengthening the electrical conductivity of ZnO. Fig. 10(f) depicts the incorporation of Mg in the ZnO host matrix.

### 3.2. Acetone sensing characteristics

It is well recognised that the sensitivity of gas sensors, based on metal oxides, is influenced by the operational temperature and humidity it is known that changes in relative humidity may alter adsorption sites and affect sensor performance. In this study, all sensor measurement were carried out in dry air and to find the ideal operating temperature, the response to 40 ppm of  $C_3H_6O$  was assessed between 200 and 400 °C. Fig. 11 illustrates the responses of M1ZO, M3ZO, and M5ZO sensors to acetone at various temperatures. The change in response as a function of





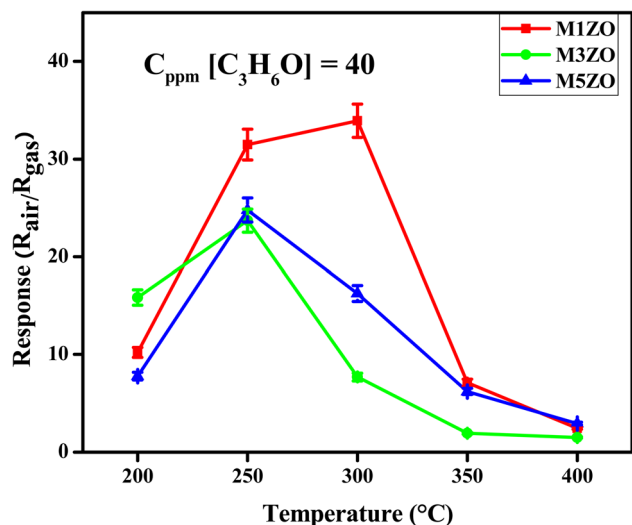


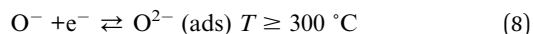
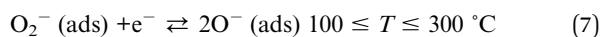
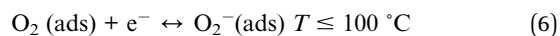
Fig. 11 Response of M1ZO, M3ZO, and M5ZO-based sensors at various operating temperatures to 40 ppm of acetone.

temperature is linked to the chemisorption and surface reaction.<sup>39</sup> For the M1ZO sensor, the response rises as the operating temperature increases and hits its peak at 300 °C, indicating the ideal temperature. Subsequently, the sensor's response decreases with further temperature rise. This behaviour can be explained as follows: The sensor's response relies on the reactivity of acetone with oxygen that is adsorbed. Up to 300 °C, the thermal energy is adequate to activate the reaction of acetone with oxygen species adsorbed on the surface. Nonetheless, increasing temperature leads to a reduction in the amount of adsorbed oxygen, which in turn causes a decrease in the gas response. The M1ZO sensor shows greater values than both M3ZO and M5ZOK: it is around 33.95 at 300 °C.

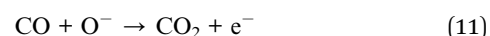
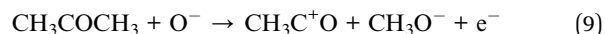
Fig. 12(a) shows the sensor's resistance of M1ZO while exposed to acetone concentrations ranging from 5 to 40 ppm. Upon the injection of the target gas (C<sub>3</sub>H<sub>6</sub>O), the resistance of the sensors drops instantly. When the acetone supply is halted, the signal reverts to the original baseline levels. Consequently, the M1ZO sensor displays a reversible n-type behaviour. The change in electrical resistance is attributed to gas adsorption and desorption occurring on the surface of the ZnO layer.<sup>40</sup> Fig. 12(b) illustrates how the response of the three sensors steadily rises as the acetone concentration rises. This validates the M1ZO sensor, which thus appears as a promising sensor for applications in the real world.

Response and recovery times are two key characteristics of gas sensors in practice. Fig. 12(c) shows the response and recovery times of the M1ZO-based sensor when exposed to 5–40 ppm acetone gas at an operating temperature of 300 °C. It can be seen that the response time decreases significantly with increasing acetone concentration, but the recovery time is the opposite; it decreases with decreasing acetone concentration. Because more gas molecules are adsorbed more quickly at higher concentrations, the reaction time diminishes while the recovery time increases because it takes longer to reestablish the baseline after more adsorbed molecules have been

desorbed. The measured reaction and recovery times are short. In fact, in the C<sub>3</sub>H<sub>6</sub>O concentration range of 5 to 40 ppm, the reaction time is less than 8 seconds, and the recovery time is less than 6 minutes (min). To evaluate the repeatability of the examined sensor, 40 ppm of C<sub>3</sub>H<sub>6</sub>O gas was injected multiple times consecutively into the test chamber, maintaining 300 °C as the operating temperature for M1ZO, M3ZO, and M5ZO. The test results obtained were presented in Fig. 12(d). This figure also demonstrates that reproducibility was assessed. It is evident that a minor variation in response is noted during the 5-cycle test. This behaviour demonstrates the strong response and remarkable repeatability of the M1ZO sensor. The gas sensing principle of resistive sensors made from semiconductor oxides mainly relies on the alterations in the sensor's resistance when exposed to target gases, attributed to the chemical interactions that occur between adsorbed oxygen ions and gas molecules. When the n-type semiconductor oxide sensors come into contact with synthetic air, oxygen molecules are adsorbed onto their surface layers. The oxygen molecules that are adsorbed take away electrons from the film's surface conduction band, leading to the creation of negatively charged oxygen ions. The types of chemisorbed oxygen ions are identified based on the operating temperature. The subsequent equations encapsulate the process of oxygen ion formation. Initially, reactive oxygen species including O<sub>2</sub><sup>−</sup>, O<sup>2−</sup>, and O<sup>−</sup> are adsorbed onto the ZnO surface at high temperatures. It is important to mention that the chemisorbed oxygen species are highly influenced by temperature. The kinematics of the reaction can be outlined as follows:<sup>41,42</sup>



The conductivity of ZnO NPs increases as reducing acetone vapour enters the test chamber due to electron exchange between the ion-adsorbed species and the ZnO itself.<sup>43</sup> The interaction of acetone with ionic oxygen species can be characterised as follows:<sup>44,45</sup>



Selectivity is one of the key parameters of gas sensors and describes the ability of the sensor to respond to a specific gas in the presence of other interfering gases. M1ZO, the sensor with the best performance, was subjected to selectivity measurement in order to effectively concentrate on the most promising sample. Fig. 12(e) shows some sensor tests of the M1ZO at 300 °C for different dangerous gases (acetone (C<sub>3</sub>H<sub>6</sub>O), ammonia (NH<sub>3</sub>), carbon dioxide (CO<sub>2</sub>), hydrogen sulfide (H<sub>2</sub>S) and sulfur



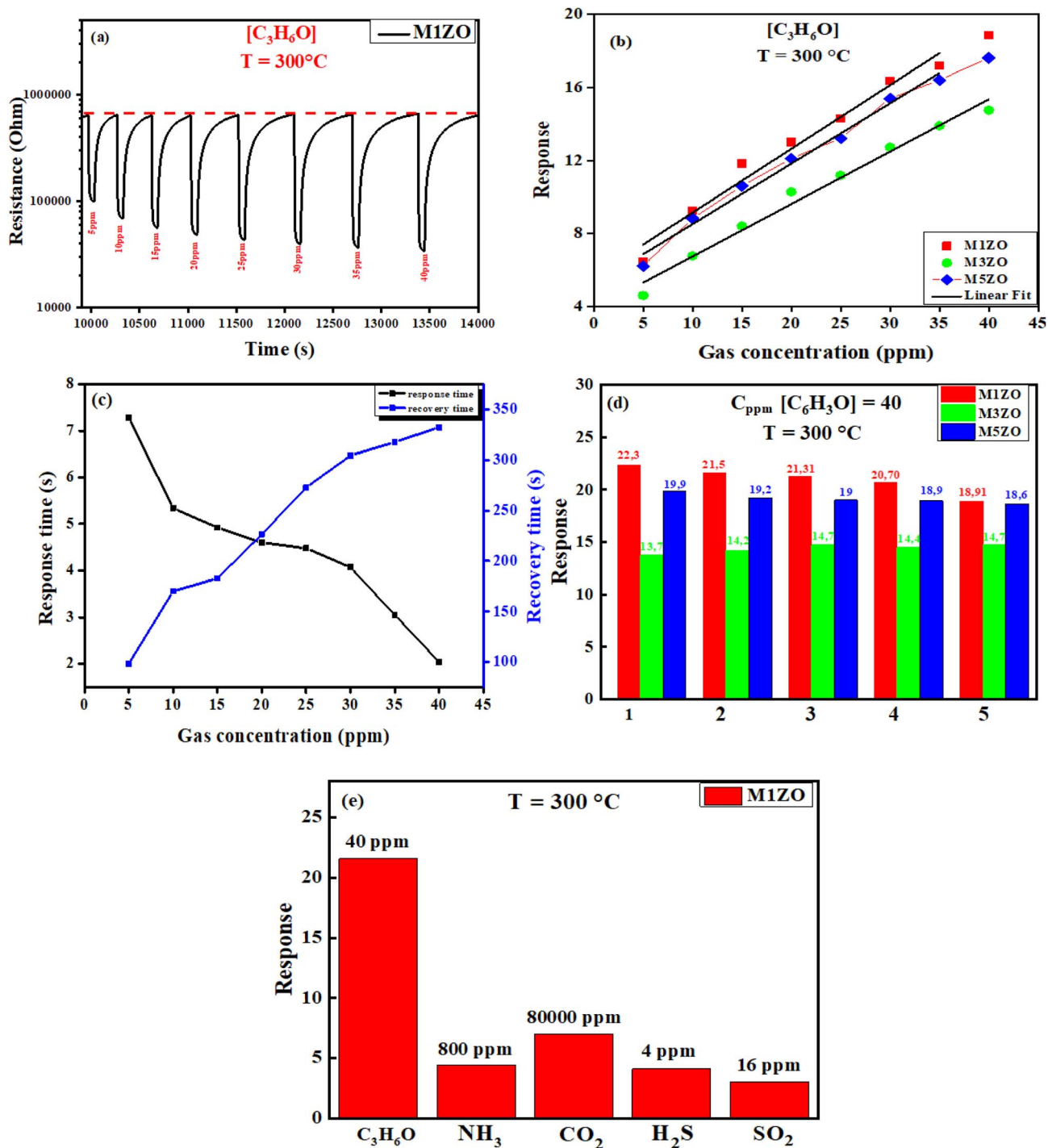


Fig. 12 (a) Response of M1ZO-based sensor to different acetone concentrations (5–40 ppm), (b) responses of M1ZO, M3ZO, and M5ZO sensors. (c) Response and recovery time versus concentration for M1ZO NPs at an operating temperature of  $300^\circ C$ . (d) Reproducibility towards 40 ppm at  $300^\circ C$  for M1ZO, M3ZO, and M5ZO-based sensors. (e) Response of M1ZO at  $300^\circ C$  to different gases, proving the selectivity for acetone.

dioxide ( $SO_2$ )). Although M1ZO was exposed to high concentrations of  $NH_3$  (800 ppm) and  $CO_2$  (80 000 ppm), it appears that, despite the excellent sensing performance of the Mg-doped ZnO sensor, the selectivity for acetone is relatively high. According to previous studies, the improved performance of the sensor based on a synthesised M1ZO sample against acetone gas is associated with various factors such as high

surface roughness, small particles, stacking defects, and the amount of oxygen vacancies. XRD results showed an increase in the size of M1ZO particles compared to undoped ZnO NPs. Therefore, the improved gas sensor performance cannot be attributed to the small particle size. UV-Vis studies showed an increase in the intensity of the absorption bands, which led to an increase in the carrier concentration. The higher number of

**Table 3** A comparison of the acetone detection properties of the 1% Mg-doped ZnO NPs sensor in this study with those from previously published studies

Sensing material	Temperature (°C)	Acetone (ppm)	Response ( $R_a/R_g$ )	Reference
Al doped ZnO	300	50	27	46
Ag/ZnO nanocomposites	175	1000	71	47
Co-doped ZnO nanofibers	360	100	16	48
Sn-doped ZnO ultra-thin nanosheet	320	200	5.5	49
Mn/ZnO microstructures	300	300	29	50
Mg-doped ZnO	300	40	19.9	This work

carriers can be considered the reason for the stronger gas response.

The sensor performance was compared with the latest studies based on ZnO-doped nanostructures. Table 3 shows the comparison of the gas sensing properties of M1ZO NPs with other sensing nanomaterials for acetone; only the metrics available in the original articles are included. As it is shown, M. Ben Amara *et al.*<sup>46</sup> synthesised a sensor based on Al-doped ZnO NPs with notable sensing properties to acetone. Even the sensor exhibited high response, but it worked at a relatively high concentration of acetone (50 ppm).<sup>47</sup> On the other hand, Liu *et al.*<sup>48</sup> used high working temperature (about 360 °C) for detection of 100 ppm acetone (high concentration). The Co-doped ZnO-based sensor shows relatively high response (16) but at higher detection and higher operating temperature. Conversely, M. H. Darvishnejad *et al.*<sup>49</sup> succeed to synthesize Mn/ZnO based sensor. The sensor was used for the monitoring of acetone (300 ppm) and showed a relatively low response (29), compared to gas concentration, at relatively higher operating temperature (300 °C). Focusing on other cited examples, which used the operating temperature of 320 °C, the synthesised Sn-doped ZnO sensor considered by Y. Al Hadeethi *et al.*<sup>50</sup> shows a considerably lower sensitivity (5.5). At 1000 (40\*25) ppm of acetone, the Ag-ZnO sensor<sup>45</sup> exhibited a response of approximately 71, which is about 3.56 times higher than the response of 19.9 (this work). Despite that, the presented M1ZO sensor shows a higher response and lower detection limit ( $\leq 5$  ppm) at 300 °C. In addition, the sensing layer was elaborated and deposited by an easier and faster method. So, the optimised 1% Mg doping, which adds oxygen vacancies and structural flaws that serve as active sites for acetone adsorption, as well as an adjusted form that boosts effective surface area, is responsible for the increased sensitivity of M1ZO. Finally, due to the simple elaboration process and excellent gas-sensing properties, the M1ZO sensor is regarded as a strong contender for effective and high detection of acetone.

## 4. Conclusion

In summary, we have successfully synthesised ZnO and MXZO ( $X = 1, 3$ , and  $5$  at%) nanoparticles *via* the sol-gel technique. The refined XRD patterns confirmed the hexagonal wurtzite structure with a  $P6_3mc$  space group for all samples. The crystallite size increased in the Mg-doped ZnO samples (44–57 nm).

TEM images revealed nanosized prismatic-shaped particles, in agreement with the XRD findings. SEM analysis displayed dispersed spherical aggregates, with a gradual increase in density upon Mg incorporation. EDX analysis confirmed the presence of Zn, O, and Mg elements with appropriate stoichiometry. The M1ZO sensor exhibited promising gas sensing characteristics, including high sensitivity ( $R_a/R_g = 19.9$  at 40 ppm and 300 °C), low detection limit ( $\leq 5$  ppm), fast response, and long-term repeatability for  $C_3H_6O$  detection. Nevertheless, ZnO and MXZO-based sensors were also evaluated for other gas detection. Preliminary results were encouraging, showing the excellent selectivity of M1ZO for acetone in contrast to the other gases. The systematic investigation of magnesium doping in ZnO, which shows that 1% Mg optimises structural flaws and morphology to improve acetone sensing capability, is what makes this work novel. In future work, efforts will focus on enhancing the four key performance parameters: sensitivity, selectivity, stability, and speed, through co-doping with the calcium (Ca) element of cologne II, like magnesium, aiming to detect a broader range of hazardous gases. Because of its higher ionic radius, which might provide more oxygen vacancies and lattice strain, Ca was chosen for future co-doping in order to potentially improve gas sensing performances.

## Author contributions

(1) MEB contributed to the sample synthesis, data analysis, and main manuscript writing. (2) and (3) NH and MJ contributed to analysis (4), (5), and (6) SJ, NMB, and FBA contributed to the conceptualisation and characterisations (7) and (8) GN, and LEM performed the supervision, reviewing, and editing of the manuscript.

## Conflicts of interest

The authors declare no conflict of interest in preparing this article.

## Data availability

The datasets generated during the current study are available from the corresponding author upon reasonable request.

Supplementary information is available. See DOI: <https://doi.org/10.1039/d5ra05067g>.



## Acknowledgements

This work was financially supported by the Tunisian Ministry of Higher Education and Scientific Research through the budget of the Tunisian Laboratories.

## References

- 1 P. Agarwal, A. Goyal and R. Vaishnav, *Asian J. Pharm. Clin. Res.*, 2018, **11**, 27–35.
- 2 P. Mainkar, A. Ray and S. Chandrasekhar, *ACS Omega*, 2024, **9**, 7271–7276.
- 3 L. Sang, G. Xu, Z. Chen, X. Wang, H. Cui, G. Zhang and Y. Dou, *Mater. Sci. Semicond. Process.*, 2020, **105**, 104710.
- 4 S. Mrabet, N. Ihzaz, M. N. Bessadok, M. Alshammari, O. M. Lemine, D. Ananias and L. El Mir, *Dalton Trans.*, 2025, **54**, 7400–7414.
- 5 O. M. Lemine, N. Madkhali, M. Alshammari, S. Algessair, A. Gismelseed, L. El Mir, M. Hjiri, A. A. Yousif and K. El-Boubbou, *Materials*, 2021, **14**, 5691.
- 6 C. Castillo, G. Cabello, B. Chornik, Y. Huentupil and G. E. Buono-Core, *J. Alloys Compd.*, 2020, **825**, 154166.
- 7 B. Bouricha, R. Souissi and L. El Mir, *Expert Syst. Appl.*, 2024, **243**, 122909.
- 8 S. Kanaparthi and S. Govind Singh, *Mater. Sci. Energy Technol.*, 2020, **3**, 91–96.
- 9 A. Kołodziejczak-Radzimska and T. Jesionowski, *Materials*, 2014, **7**, 2833–2881.
- 10 Z. Ben Ayadi, H. Mahdhi, K. Djessas, J. L. Gauffier, L. El Mir and S. Alaya, *Thin Solid Films*, 2014, **553**, 123–126.
- 11 J. Xuan, G. Zhao, M. Sun, F. Jia, X. Wang, T. Zhou, G. Yin and B. Liu, *RSC Adv.*, 2020, **10**, 39786–39807.
- 12 M. Amin, N. A. Shah, A. S. Bhatti and M. A. Malik, *Cryst. Eng. Comm.*, 2014, **16**, 6080–6088.
- 13 R. Dhahri, M. Hjiri, L. E. Mir, A. Bonavita, D. Iannazzo, S. G. Leonardi and G. Neri, *Appl. Surf. Sci.*, 2015, **355**, 1321–1326.
- 14 R. Dhahri, M. Hjiri, L. El Mir, A. Bonavita, D. Iannazzo, M. Latino, N. Donato, S. G. Leonardi and G. Neri, *J. Phys. D Appl. Phys.*, 2016, **49**, 135502.
- 15 S. Jaballah, Y. Alaskar, I. AlShunaifi, I. Ghiloufi, G. Neri, C. Bouzidi, H. Dahman and L. El Mir, *Chemosensors*, 2021, **9**, 300.
- 16 N. Khelifi, N. Ihzaz, O. Toulemonde, A. Dandre, C. Labrugère-Sarroste, M. N. Bessadok, O. M. Lemine and L. El Mir, *RSC Adv.*, 2024, **14**, 27622–27633.
- 17 S. Jaballah, H. Dahman, G. Neri and L. El Mir, *J. Inorg. Organomet. Polym. Mater.*, 2021, **31**, 1653–1667.
- 18 H. Dahman and L. El Mir, *J. Mater. Sci. Mater. Electron.*, 2015, **26**, 6032–6039.
- 19 S. Mrabet, N. Ihzaz, M. N. Bessadok, C. Vázquez-Vázquez, M. Alshammari and L. El Mir, *J. Inorg. Organomet. Polym. Mater.*, 2024, **34**, 2064–2073.
- 20 B. C. Lippens and J. H. De Boer, *J. Catalysis*, 1965, **4**, 319–323.
- 21 S. Muthukumaran and R. Gopalakrishnan, *Opt. Mater.*, 2012, **34**, 1946–1953.
- 22 M. Rouchdi, E. Salmani, B. Fares, N. Hassanain and A. Mzerd, *Results Phys.*, 2017, **7**, 620–627.
- 23 R. E. Adam, H. Alnoor, G. Pozina, X. Liu, M. Willander and O. Nur, *Solid State Sci.*, 2020, **99**, 106053.
- 24 X. Si, Y. Liu, X. Wu, W. Lei, J. Lin, T. Gao and L. Zheng, *Phys. Lett. A*, 2015, **379**, 1445–1448.
- 25 S. Jaballah, M. Benamara, H. Dahman, A. Ly, D. Lahem, M. Debliquy and L. El Mir, *Mater. Chem. Phys.*, 2020, **255**, 123643.
- 26 N. Al Dahoudi, A. AlKahlout, S. Heusing, P. Herbeck-Engel, R. Karos and P. Oliveira, *J. Sol-Gel Sci Technol.*, 2013, **67**, 556–564.
- 27 K. Vijayalakshmi and A. Renitta, *J. Mater. Sci. Mater. Electron.*, 2015, **26**, 3458–3465.
- 28 R. Slama, J. El Ghoul, K. Omri, A. Houas, L. El Mir and F. Launay, *J. Mater. Sci. Mater. Electron.*, 2016, **27**, 7939–7946.
- 29 L. El Mir, Z. B. Ayadi, M. Saadoun, J. von Bardeleben, K. Djessas and A. Zeinert, *Phys. Status Solidi A*, 2007, **204**, 3266–3277.
- 30 J. El Ghoul, C. Barthou and L. El Mir, *Superlattices Microstruct.*, 2012, **51**, 942–951.
- 31 F. Hussain, M. Imran, R. M. A. Khalil, N. A. Niaz, A. M. Rana, M. A. Sattar, M. Ismail, A. Majid, S. Kim, F. Iqbal, M. A. Javid, S. Saeed and A. Sattar, *Phys. E*, 2020, **115**, 113658.
- 32 J. Singh, P. Kumar, K. S. Hui, K. N. Hui, K. Ramam, R. S. Tiwari and O. N. Srivastava, *CrystEngComm*, 2012, **14**, 5898–5904.
- 33 J. G. Lu, Z. Z. Ye, Y. J. Zeng, L. P. Zhu, L. Wang, J. Yuan, B. H. Zhao and Q. L. Liang, *J. Appl. Phys.*, 2006, **100**, 73714.
- 34 G. El Hallani, S. Nasih, N. Fazouan, A. Liba, M. Khuili, M. Sajieddine, M. Mabrouki, L. Laanab and E. H. Atmani, *J. Appl. Phys.*, 2017, **121**, 135103.
- 35 A. J. Kulandaisamy, J. R. Reddy, P. Srinivasan, K. J. Babu, G. K. Mani, P. Shankar and J. B. B. Rayappan, *J. Alloys Compd.*, 2016, **688**, 422–429.
- 36 W. Cheng, P. Wu, X. Zou and T. Xiao, *J. Appl. Phys.*, 2006, **100**, 54311.
- 37 T. M. Børseth, B. G. Svensson, A. Y. Kuznetsov, P. Klason, Q. X. Zhao and M. Willander, *Appl. Phys. Lett.*, 2006, **89**, 262112.
- 38 Y. Zong, Y. Sun, S. Meng, Y. Wang, H. Xing, X. Li and X. Zheng, *RSC Adv.*, 2019, **9**(40), 23012.
- 39 J. Sun, S. Bai, Y. Tian, Y. Zhao, N. Han, R. Luo, D. Li and A. Chen, *Sens. Actuators, B*, 2018, **257**, 29–36.
- 40 X. Liu, J. Zhang, L. Wang, T. Yang, X. Guo, S. Wu and S. Wang, *J. Mater. Chem.*, 2011, **21**, 349–356.
- 41 A. L. Zou, Y. Qiu, J. J. Yu, B. Yin, G. Y. Cao, H. Q. Zhang and L. Z. Hu, *Sens. Actuators, B*, 2016, **227**, 65–72.
- 42 M. Sudha, S. Radha, S. Kirubaveni, R. Kiruthika, R. Govindaraj and N. Santhosh, *Solid State Sci.*, 2018, **78**, 30–39.
- 43 Z. Yuan, Z. Feng, L. Kong, J. Zhan and X. Ma, *J. Alloys Compd.*, 2021, **865**, 158890.
- 44 S. Zhang, P. Song, L. Liu, Z. Yang and Q. Wang, *Ceram. Int.*, 2017, **43**, 7942–7947.
- 45 D. Degler, S. Wicker, U. Weimar and N. Barsan, *J. Phys. Chem. C*, 2015, **119**, 11792–11799.





- 46 M. Benamara, P. Rivero-Antúnez, H. Dahman, M. Essid, S. Bouzidi, M. Debliquy, D. Lahem, V. Morales-Flórez, L. Esquivias, J. P. B. Silva and L. El Mir, *J. Sol-Gel Sci. Technol.*, 2023, **108**, 13–27.
- 47 D. Y. Nadargi, R. B. Dateer, M. S. Tamboli, I. S. Mulla and S. S. Suryavanshi, *RSC Adv.*, 2019, **9**, 33602–33606.
- 48 L. Liu, S. Li, J. Zhuang, L. Wang, J. Zhang, H. Li, Z. Liu, Y. Han, X. Jiang and P. Zhang, *Sens. Actuators, B*, 2011, **155**, 782–788.
- 49 M. H. Darvishnejad, A. Anaraki Firooz, J. Beheshtian and A. A. Khodadadi, *RSC Adv.*, 2016, **6**, 7838–7845.
- 50 Y. Al-Hadeethi, A. Umar, S. H. Al-Heniti, R. Kumar, S. H. Kim, X. Zhang and B. M. Raffah, *Ceram. Int.*, 2017, **43**, 2418–2423.

